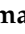




Article

Effect of Lateral Laser-Cladding Process on the Corrosion Performance of Inconel 625

Mohammad Rezayat ¹, Amirhossein Aboutorabi Sani ², Mohammad Talafi Noghani ², Morteza Saghafi Yazdi ², Morteza Taheri ³, Amirhossein Moghanian ², Mohammad Abedini Mohammadi ², Mahmoud Moradi ⁴, Antonio Manuel Mateo García ^{1,5} and Hossein Besharatloo ^{1,5,6,*}

¹ Center for Structural Integrity, Micromechanics, and Reliability of Materials (CIEFMA)-Department of Materials Science and Engineering, Universitat Politècnica de Catalunya-BarcelonaTECH, 08019 Barcelona, Spain

² Department of Materials Engineering, Imam Khomeini International University, Qazvin 34149-16818, Iran

³ Department of Material Engineering, South Tehran Branch, Islamic Azad University, Tehran 1459853849, Iran

⁴ Faculty of Arts, Science and Technology, University of Northampton, Northampton NN1 5PH, UK

⁵ Barcelona Research Center in Multiscale Science and Engineering, Politècnica de Catalunya BarcelonaTECH, 08019 Barcelona, Spain

⁶ Institute of Ceramic and Glass—CSIC, 28049 Madrid, Spain

* Correspondence: Hossein.Besharatloo@upc.edu

Abstract: This study aimed to evaluate the corrosion properties of different samples coated by the laser-cladding method to find the optimal laser parameters. Thereby, potentiodynamic polarization (Tafel) and electrochemical impedance tests were performed to assess the corrosion resistance of coated samples. Consequently, the corrosion morphology of tested samples was inspected by scanning electron microscopy. The results demonstrated that the laser power directly correlates with pitting corrosion and defects on the surface of the samples. Moreover, when molybdenum and chromium ions are increased in the electrolyte solution, the passive and protective layers are more durable, as the ions are sited within the holes and defects, reducing the surface corrosion rate.

Keywords: laser cladding; corrosion; Inconel 738; Inconel 625; Nyquist; Tafel



Citation: Rezayat, M.; Aboutorabi Sani, A.; Talafi Noghani, M.; Saghafi Yazdi, M.; Taheri, M.; Moghanian, A.; Mohammadi, M.A.; Moradi, M.; Mateo García, A.M.; Besharatloo, H. Effect of Lateral Laser-Cladding Process on the Corrosion Performance of Inconel 625. *Metals* **2023**, *13*, 367. <https://doi.org/10.3390/met13020367>

Academic Editor: Lai-Chang Zhang

Received: 20 December 2022

Revised: 2 February 2023

Accepted: 9 February 2023

Published: 11 February 2023



Copyright: © 2023 by the authors. Licensee MDPI, Basel, Switzerland. This article is an open access article distributed under the terms and conditions of the Creative Commons Attribution (CC BY) license (<https://creativecommons.org/licenses/by/4.0/>).

1. Introduction

Inconel 738 is a nickel-based superalloy, which are mainly used in aerospace [1–4] and oil industries [5], thanks to their excellent properties such as fatigue resistance, high yield strength, corrosion resistance, and thermal stability [6]. The mechanical properties of Inconel 738 superalloy depend on microstructural parameters such as the volume fraction of the intermetallic γ' -phase ($\text{Ni}_3(\text{Al}, \text{Ti})$) and also on the dimensions, distribution, and shape of γ' particles [7–9]. However, gas turbine evolution leads to increasingly higher service temperatures, and corrosion problems often appear [1,2]. Different coatings have been evaluated to enhance corrosion properties; for example, coatings for high-temperature applications include diffusion and thermal barrier coatings [10].

Inconel 625 is widely used as a coating material for corrosive environments owing to its high content of chromium, nickel, and molybdenum [11–13], which guarantees outstanding corrosion and oxidation resistance [14]. Inconel 625 is also a good coating for marine environments and cutting tools [15]. Therefore, the use of oxidation-resistant coatings, such as Inconel 625, is foreseeable to prevent severe damage to sensitive components of gas turbines [16]. In this study, Inconel 625 nickel-based superalloy has been coated on Inconel 738 substrate by lateral laser cladding.

Nowadays, several surface coating methods are available, such as mechanical [17], chemical [18–21], sol-gel [22], oxidation [23,24], carburization [25], ion implantation [26,27], thermal [28,29], and cladding methods [30]. Laser cladding (LC) is an advanced surface modification technique [31,32] that is commonly used in industrial applications, such

as rapid manufacturing, repair and maintenance, and the development of innovative materials such as functionally graded materials [33,34]. A relatively thick (50 μm to 2 mm) and homogeneous overlay of coating material can be produced with the aid of LC [35,36], creating a very smooth surface with the desired roughness, as the amount of geometric dilution of the coating produced by LC is higher than with other methods [37].

Cabrini et al. [38] investigated cyclic polarization and potentiodynamic tests to evaluate the corrosion resistance of different alloys based on ASTM G5 by laser cladding in NaCl 0.6 M solution at pH 7 and pH 3 at 40 °C. A correlation between corrosion performance and microstructure has also shown an increase in the corrosion resistance of surfaces made after laser cladding. Corrosion behaviours of stainless steel 316 and Inconel 625 alloy in NaCl were investigated by immersion tests and electrochemical methods, including potentiodynamic polarization and electrochemical impedance spectroscopy. The results of electrochemical tests showed that both in chloride show active corrosion, and the current density of 316 in chloride at 700 °C is 2.756 mA/cm², which is almost three times the value of Inconel. The corrosion of these two alloys is due to the preferential oxidation of chromium in the chloride, and the passive layer was porous and showed weak adhesion to the materials [39].

Abe et al. [40] evaluated the corrosion resistance of the Inconel 625 coating prepared by LC and found that it was free from preliminary cracks and could fully protect the stainless-steel substrate. The mentioned study only dealt with the variables of lateral laser cladding; however, in the current work, more efforts have been dedicated to investigating the corrosion properties of Inconel 625 coating and the influence of laser power on polarization corrosion tests.

2. Materials and Experimental Procedures

2.1. Materials

Inconel 738 sheets coated with Inconel 625 were investigated in the current study. Both Inconel 738 sheets and Inconel 625 powder were supplied by Huanhai alloy (Shandong, China). The chemical composition of the Inconel 738 (substrate) and Inconel 625 (powder) are shown in Table 1.

Table 1. Chemical composition of Inconel 625 powder and Inconel 738 substrate, in weight percentages.

Materials	Ni	Cr	Co	Mo	Al	Ti	Ta	Nb
Substrate Inconel 738	Bal	16.4	4.1	1.7	3.8	3.4	2.8	0.3
Powder Inconel 625	Bal	21.3	1.3	8.1	2.4	0.3	0.0	6.1

2.2. Preparation and Process of Laser Cladding

The surface of the substrates (20 × 20 × 1 mm³) was grounded with 1200 grit sandpaper and was cleaned with acetone to remove greases and impurities prior to the laser-cladding process. The laser-pulsed device Nd: YAG model IQL-10 (Quantel, Paris, France) was used to perform the coating. The laser specifications were as follows: a wavelength of about 1064 (nm), a peak power of 400 (W), energy per pulse of 8 (J), a pulse frequency of 20 (Hz), a pulse width of 20 (ms), and a pulse period of 50 (ms) (Figure 1a). The nozzle head was located at an angle of 30 degrees from the surface, the distance between the nozzle head and the workpiece surface (stand-off distance) was 80 (mm), the distance between the focal plane and the sample surface (defocused distance) was 20 (mm), and a laser beam spot diameter of 1 (mm) with 85 (%) percentage of overlapping was used (Figure 1b). During laser cladding, argon gas with a flow rate of 10 (litres/min) was blown in parallel with the direction of the injected powder nozzle on the surface (Figure 1c). Laser parameters to achieve the cladding process are summarized in Table 2.

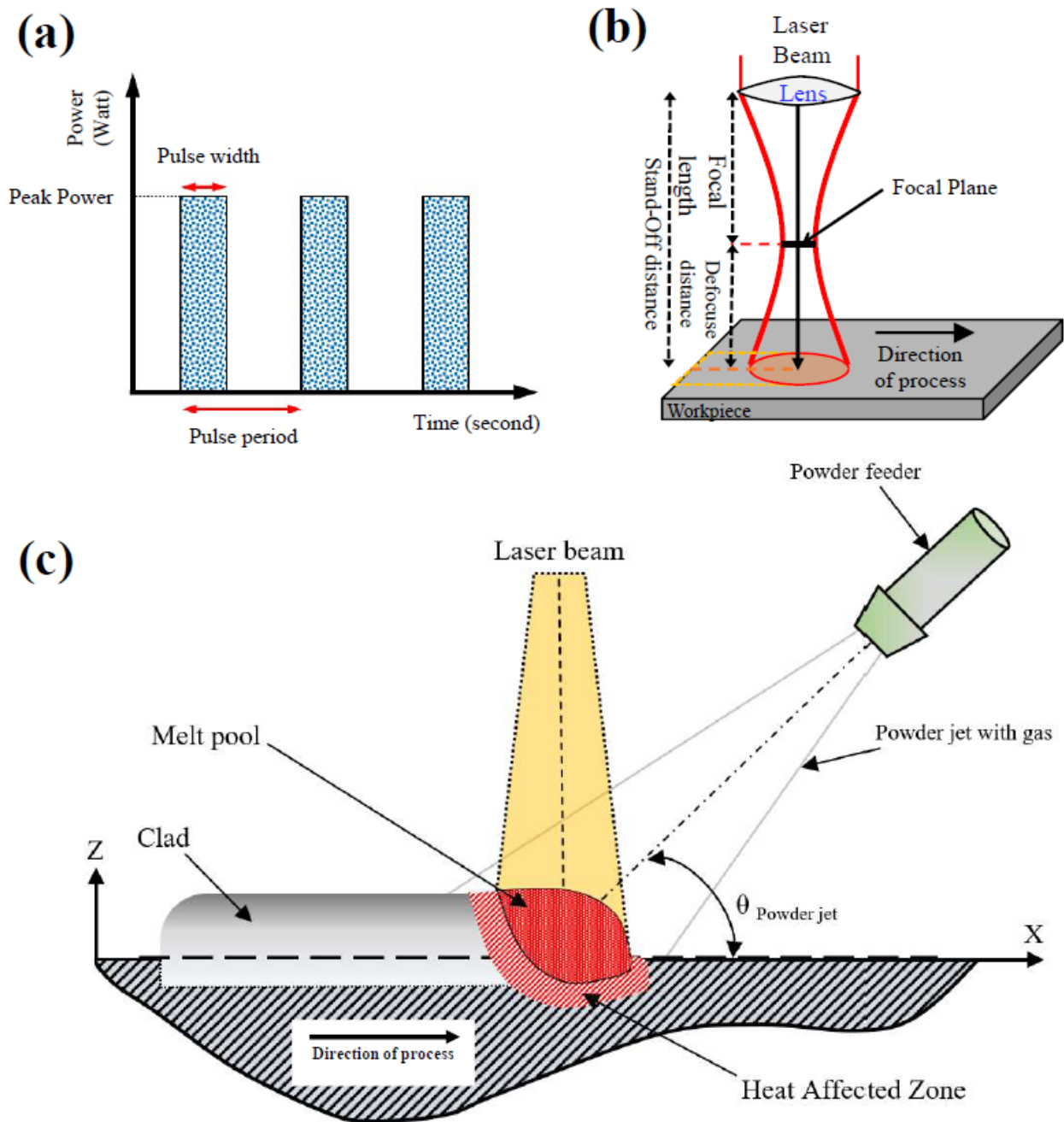


Figure 1. (a) Schematic of lateral laser cladding process in this study, (b) laser pulse diagram, (c) schematic diagram of focal plane position and stand-off distance relative to the surface of the workpiece.

Table 2. Lateral laser cladding process parameters.

Laser Scanning Rate (mm/s)	Powder Feed Rate (mg/s)	Laser Power (W)	Sample Code
5	350	150	S1
5	350	200	S2
5	350	300	S3

2.3. Microstructural Characterization

Optical microscope (OM) OLYMPUS model BX-51M (Tokyo, Japan) was used for imaging the cross-sectional surface. Marble etchant solution (FeCl_3 (1 g), HNO_3 (4 mL), and HCl

(10 mL)) was used at room temperature to etch the samples on the surface and the substrate. The dwell time was about 5 s. Field emission scanning electron microscopy (FE-SEM) (MIRA3-TESCAN, Kohoutovice, Czech Republic) was used to inspect the microstructure of the coating. ImageJ software 1.53t (Wayne Rasban, USA) was used to calculate the geometric dimensions of each coat created after laser cladding.

The X-ray diffraction equipment (Philips model Empyrean Alpha, Lelyweg, The Netherlands) was utilized to identify the phases in the coating. CuK α beam with a current of 30 mA and a wavelength of 1.542 Å at a voltage of 40 kW was used in all tests, and the phases in the X-ray diffraction pattern obtained from the samples were identified by Xpert High Score software 3.0e (PANalytical, The Netherlands).

Potentiodynamic polarization tests were used to investigate the corrosion behaviour of Inconel 738 and Inconel 738 coated with Inconel 625. The tests were performed based on the instructions stated in the ASTM standards, G5-94 and G61-86 [41], respectively. In this regard, several square-shaped samples with dimensions of 4 × 6 mm² and a thickness of 2 mm from laser-coated sheets with specific conditions were cut with a wire cutter. Subsequently, copper wires were joined on the samples with the help of a soldering machine. The cut parts were connected, except for the surface on which the corrosion test was intended to be performed. The square shape of the samples was exposed to a saline environment (3.5% NaCl) at room temperature using a three-electrode cell. Each sample (i.e., the working electrode) was immersed in the electrolyte for 20 min before polarizing the potential against the reference electrode (Saturated Calomel HgCl). A platinum electrode was used as the counter electrode. Using a potentiostat (Vertex, Ivium, The Netherlands), potentiodynamic polarization scans were performed for each sample with a scan rate of 2 mV/s from the open circuit potential (OCP) for 30 min. The potential was scanned in the range of −2 to +4 V for each sample. An open circuit system was used for the impedance electrochemical tests from 100 kHz to 10 mHz with an amplitude of 5 mV. The ZView® software 4 (Scribner, USA) chose an equivalent circuit for the analysis of impedance data.

3. Results and discussion

3.1. Cross-Section Study of Laser Cladding Samples

Figure 2 shows the affected area in the corrosion test, the corrosion zone (CZ) in green, and the area affected by the laser input heat on the surface, the heat affected zone (HAZ) in red. The laser beam is able to change this HAZ region in terms of microstructural properties and penetrate to this depth.

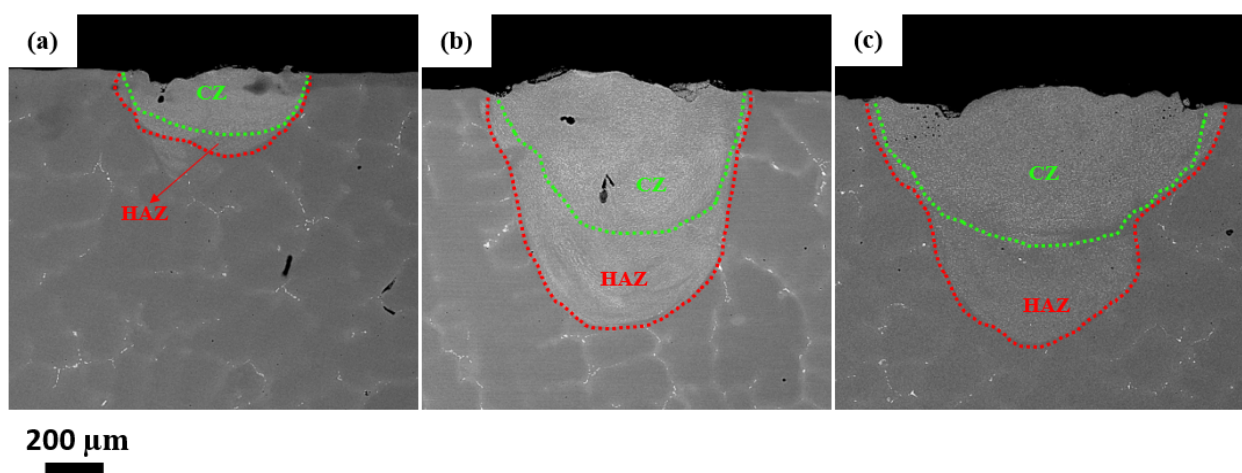


Figure 2. Optical cross-section images of Inconel 625 samples. (a) S1:150 W, (b) S2:200 W, (c) S3:300 W.

The geometry of laser-affected zones of the Inconel 625 samples (Figure 2 and Table 3) demonstrates a direct relationship between the laser power and the heat input H (J/mm^2) on the melting pool. Accordingly, the HAZ expands by raising the average laser power, due to the higher concentration of heat input and the laser energy density on the surface. Moreover, reducing the laser power can cause less penetration in the substrate, and hence a poor adhesion of the coating, which means that corrosion will occur at a higher rate.

Table 3. Geometrical dimension of laser affected zone in treated samples.

Sample	Depth of HAZ (μm)	Width of HAZ (μm)	Thickness of the Coating (μm)
S1	164.10	389.74	173.56
S2	495.72	676.92	223.13
S3	540.17	741.88	314.23

These obtained results are in agreement with those reported by Verdi et al. [42].

Equations (1) and (2) [29,43] confirm the influence of average laser power on heat input in the molten pool:

$$P_{av} = \text{Peak Power} \times D \times f \quad (1)$$

$$H = P_{av}/V \quad (2)$$

where P_{av} : average laser peak power (W), D : Pulse duration (ms), f : Pulse frequency (Hz), H : Input heat (J/mm^2), and V : Scanning speed (mm/s) are defined in these equations. Table 4 presents the calculated values for each sample. Accordingly, the measured parameters reveal that the magnitude of the thermal shock in the molten pool is directly related to its increased heat input [44,45].

Table 4. Laser parameters and heat input for each average laser power.

Sample	D (ms)	f (Hz)	V (mm/s)	P_{av} (W)	H (J/mm^2)
S1	5	20	6	150	25
S2	5	20	6	200	34
S3	5	20	6	300	50

3.2. Phase Identification

The XRD spectrums of all studied samples are presented in Figure 3, where the γ' -Ni phase is the main phase.

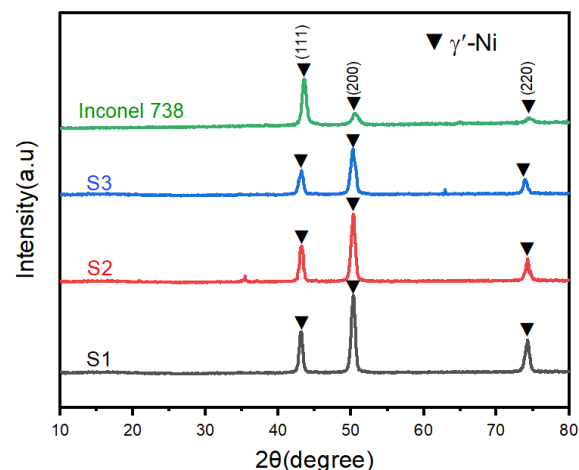


Figure 3. XRD patterns of the samples coated by laser cladding and substrate; Green: Inconel 738, Blue: S3, Red: S2, Black: S1.

The γ' -Ni phase peaks in Inconel 625 coatings appeared in all samples but with different intensities. The major peak positions in the spectrum were found for pure nickel, (111), (200), and (220), appearing at 42° , 50° , and 73° , respectively. The difference in the lattice parameter is due to alloying elements in Inconel 625, as these elements affect the inter-planar spacing of the γ' -Ni phase in the coating [46–50].

3.3. Corrosion Behavior of Inconel 625 Coating

The corrosion parameters obtained from the potentiodynamic polarization test are summarized in Table 5.

Table 5. Polarization parameters of different samples for corrosion testing in 3.5 wt% NaCl solution at room temperature. E_{corr} : Corrosion potential (V), I_{corr} : Corrosion current density (A/cm^2), R_p : Polarization resistance (Ω), β_a : anodic branch slope, β_c : Cathodic branch slope, C. Rate: Corrosion rate (mm/year).

Sample Code	E_{Corr} (V)	I_{Corr} ($\mu\text{A}/\text{cm}^2$)	R_p (Ω/cm^2)	β_a ($\text{V}\cdot\text{dec}^{-1}$)	β_c ($\text{V}\cdot\text{dec}^{-1}$)	C. Rate (mm/Year)
S1	−0.8509	2.289	2.094×10^4	0.264	0.190	0.007489
S2	−0.3903	0.859	1.650×10^4	0.036	0.311	0.002812
S3	−0.6606	3.880	1.229×10^4	0.243	0.200	0.012693
Uncoated	−0.9050	1.985	1.502×10^4	0.197	0.105	0.006494

To evaluate the corrosion resistance, a potentiodynamic polarization method was used for the samples in a 3.5% NaCl solution. Figure 4 shows the Tafel polarization curves. cathodic (β_c) and anodic (β_a) branches were used to gain the corrosion current density (Table 5). Low corrosion current density (I_{Corr}) indicates a slow corrosion rate or excellent corrosion resistance. It can be seen that the cathodic polarization process of the samples is the same. The uncoated samples S1 and S3 show extensive active dissolution behaviour after a small passivation step in the anodic polarization region. However, it can be seen that the S2 sample has a wide deactivation region in the anodic polarization region. The obtained results evince that sample S2 provides better corrosion resistance due to a less negative corrosion potential and lower corrosion current density. The passive layer formation in sample S2 took place more quickly as a consequence of a lower corrosion current density. Additionally, some researchers have pointed out that the good corrosion resistance of Inconel 625 alloy is due to the high content of Mo, Cr, Ni, and Nb, which causes the formation of a stronger passive film on the coating surface [51–53]. As can be seen in Table 6, the content of these elements in sample S2 is higher than other samples, which may be the reason for the better corrosion resistance of this sample than other samples. As can be seen in Figure 4, the formation of inactive film in sample S2 occurred at a lower current density. The formation of inactive film at lower current density prevents the severe loss of material at higher current density, which also indicates the improvement in corrosion resistance in the S2 sample. Therefore, the performed Inconel 625 coating on sample S2 provides optimal protection against corrosion in the electrolyte solution (3.5% NaCl) at room temperature. Moreover, the measured corrosion current (I_{Corr}) for sample S2 indicates that the passive layer formed has a better condition compared with other studied samples; hence, better corrosion resistance is expected for sample S2. The Tafel diagram (Figure 4) shows the relationship between the current generated in an electrochemical cell and the electrode potential of a specific metal. The Tafel curves of S3 and S1 samples display a rapid decrease in their surface corrosion resistance, which might be related to corrosion caused by chloride ions with severe damage to the passive layer [54]. The corrosion resistance behaviour of the samples improved at the beginning of the corrosion process as a result of the formation of a passive layer of nickel oxide (NiO) [55,56]. According to the Tafel diagram of sample S2 (shown in Figure 4), the passing current decreased more slowly than in other samples, and consequently, the current reached a plateau. The low passing current in sample S2 confirms that the thickness of the protective layer is preserved, and the surface

is less corroded. The presented Tafel diagram displayed that the change in potential has led to a sudden change in the current density value for all samples except S2, which verifies the inappropriateness of the passive layer formed on the Inconel 625 coating.

Table 6. EDS analysis for the zones determined in Figure 5a–d.

Other Elements (Wt%)	Nb (Wt%)	Mo (Wt%)	Cr (Wt%)	Ni (Wt%)	Zone
58.18	2.12	1.34	3.43	35	A-S1
15.89	6.24	10.87	22.63	45	B-S2
57.49	0.74	0.01	3.82	38	C-S3
46.27	0.02	2.41	6.31	45	D-Uncoated

According to the results of the Tafel test, polarization resistance was calculated using the following equation [57].

$$R_p = \beta_a \times \beta_c \div (2.3 \times (\beta_a + \beta_c) \times I_{\text{corr}}) \quad (3)$$

In Equation (3), R_p is polarization resistance, β_a is anodic Tafel slope, β_c is cathodic Tafel slope and I_{corr} is corrosion current. R_p values for different samples are shown in Table 5. As can be seen, the results are consistent with other corrosion tests. Based on the calculated values, the S2 sample has the most optimal polarization resistance along with low corrosion current.

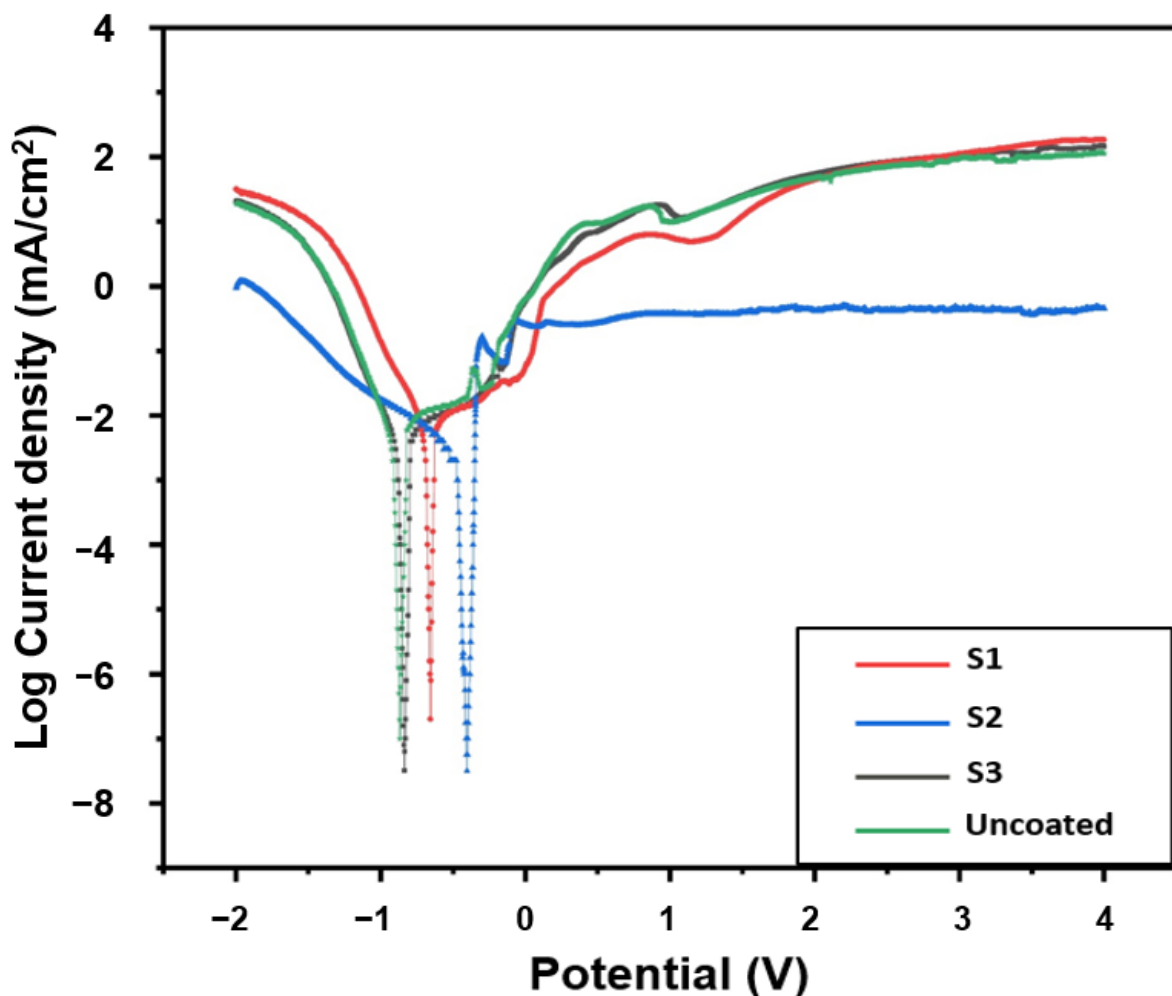


Figure 4. Potentiodynamic polarization (Tafel) curves of the samples: S1, S2, S3, and Uncoated sample.

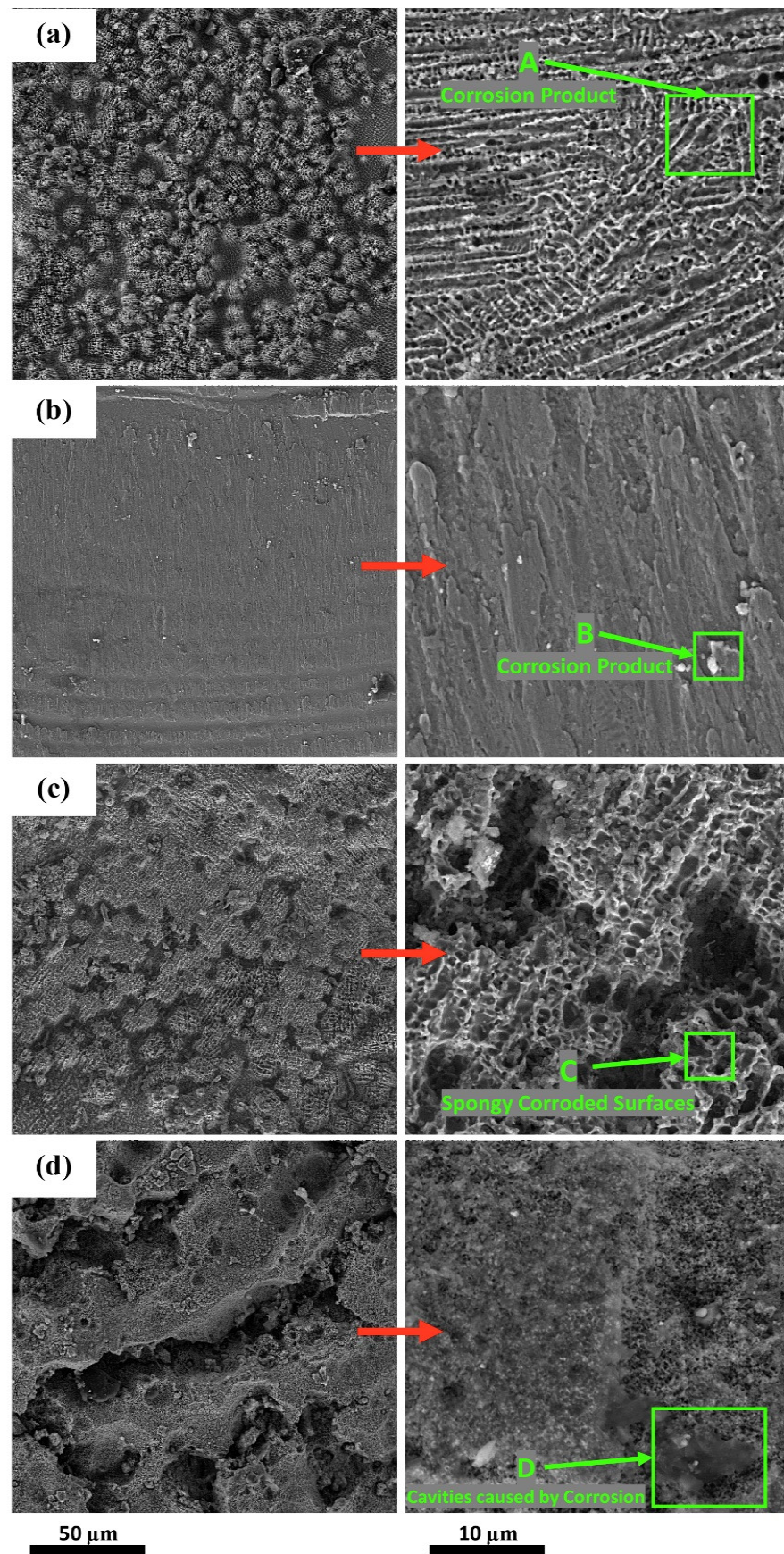


Figure 5. Images of the surface of the samples after corrosion: (a) S1, (b) S2, (c) S3, (d) Uncoated.

Figure 5 shows SEM micrographs taken from the surface of all studied samples after the corrosion test. There are two main reasons for the corrosion in the coating: (i) the formation of a non-uniform passive layer on the coating, and (ii) the improper fixation and placement of the Inconel 625 coating on the Inconel 738 substrate. Figure 5b shows a quite different aspect for sample 2, as compared with the other samples, with very limited and localized corrosion points. This shows that a uniform layer of Inconel 625 coating with the appropriate thickness was placed on sample S2. Such a behaviour can be rationalized by the higher amount of molybdenum found on Inconel 625 laser coating on the S2 sample (Table 6). The presence of molybdenum ions in the coating surface's cavities helps to protect the coating against pitting corrosion by forming sodium molybdate, as a result of the reaction of sodium in the polarization solution with molybdenum [58]. Similar behaviour was observed regarding the anti-corrosion properties of (S235JR) steel with Inconel 625 laser cladding coatings elsewhere [59,60].

As can be seen in Figure 5a,c, pitting and groove corrosion severely damaged the coating surface of samples S1 and S3, respectively. The presence of corrosion products and crevice corrosion caused the surface to become spongy in some places, which was confirmed by the SEM images. A, B, C, and D areas in Figure 5 were analysed by energy dispersive spectrometry (EDS), and the results are displayed in Table 6. The molybdenum and chromium elements are critical parameters for corrosion behaviour as ions are absorbed into the formed holes and protect the surface against pitting corrosion. Accordingly, the surface corrosion rate decreased for the S2 sample, as it contains a higher amount of chromium and molybdenum within the electrolyte solution (see Tables 5 and 6). In addition, the amount of these protective coating elements in the uncoated sample is remarkable. The uncoated sample contains a significant amount of Ti element, which improves the hardness of the alloy against wear, but increases the susceptibility of the alloy to corrosion [61]. The purpose of applying the coating is to increase the corrosion resistance of the alloy by increasing the amount of Mo, Cr, and Nb elements on the surface of the alloy. For this reason, the application of Inconel 625 coating, in addition to maintaining the mechanical strength of the alloy, significantly improves its corrosion resistance. The chromium and molybdenum in sample S3 were oxidized after receiving the highest average laser power, which reduces the corrosion rate (Tables 5 and 6) [48]. The corrosion process was initiated with the passive layer's local failure, and the localized corrosive attack can be originated in the Inconel 738 substrate (Figure 5c). While uniform corrosion can be seen on the surface, pitting corrosion mainly appears as small holes. The amount of material removed underneath the holes is generally unknown because hidden pits can form, making pitting corrosion more difficult to detect and/or predict [62]. Various forms of corrosion are evident in the microscopic images, which apply to pitting corrosion. The through pits were seen as shallow and elliptical (Figure 5a), and sideway pits occurred in the subsurface due to the increase in average laser power (Figure 5c) [63].

Among the reasons for the spongy spots, the selectiveness of the corrosion site on the coating can be identified, as well as the improper stabilization and placement of the Inconel 625 coating on the Inconel 738 substrate, and the formation of a non-uniform layer on the coating.

The pH of corrosive solution around the Inconel 738 substrate greatly affects the corrosion of the Inconel 625 coating [59]. The pH of the polarization solution is increased when nickel ions are added to the polarization solution. According to Figure 6, related to the electrochemical phase diagram for nickel (Pourbaix diagram), nickel oxide is a passive coating-resistant layer at high pH [64].

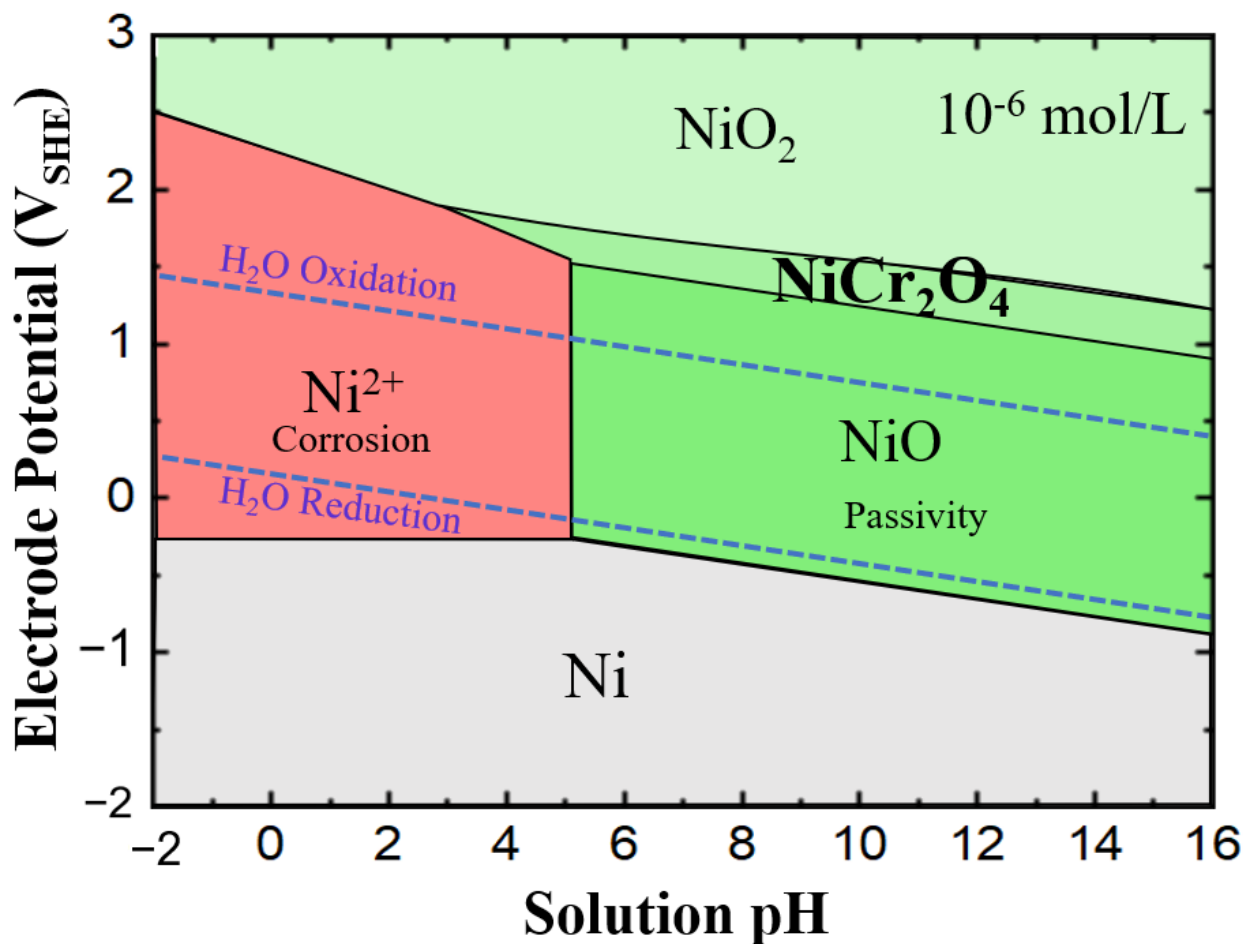


Figure 6. Electrochemical phase diagram (Pourbaix) for nickel oxidation [64].

The spinel phase (NiCr_2O_4), which prevents oxygen from entering the coating, is not included in the Inconel 625 surface at low pH [65]; accordingly, the corrosion resistance increased [66]. The Inconel 738 substrates without Inconel 625 coating are also resistant to corrosion [67–69]; however, the coated sample S2 has a lower corrosion rate than the uncoated substrate owing to a proper formation of a passive nickel layer on the surface of S2 sample.

Figure 7 represents the impedance spectra for Nyquist plots by fitting the experimental data to the equivalent circuit model. Based on Figure 7 curves, capacitive semi-circular loops are similar in shape for samples, although the diameters are different. Increasing the diameter of the Nyquist diagrams shows the high charge transfer resistance (R_{ct}). In total, a larger diameter in the semicircle in the Nyquist curve means better corrosion resistance. As can be seen, the S2 sample has the highest charge transfer resistance and the highest corrosion resistance. Additionally, if the peak frequency of these semicircles is measured, the amount of corrosion capacitance can be calculated using Equation (4):

$$[Z' - (R_s + R_p/2)]^2 + (Z'')^2 = (R_p/2)^2 \quad (4)$$

Equation (5) is for the circle with a centre of $(R_s + R_p/2) Z'$ located on the Z' axis, and its radius is $R_p/2$. At the circle peak (maximum value $| -Z'' |$), it can be shown that by differentiating from $-Z''$ respect to Z' and equating to zero:

$$CdI = 1/\omega_j.Z | -Z'' | \max \quad (5)$$

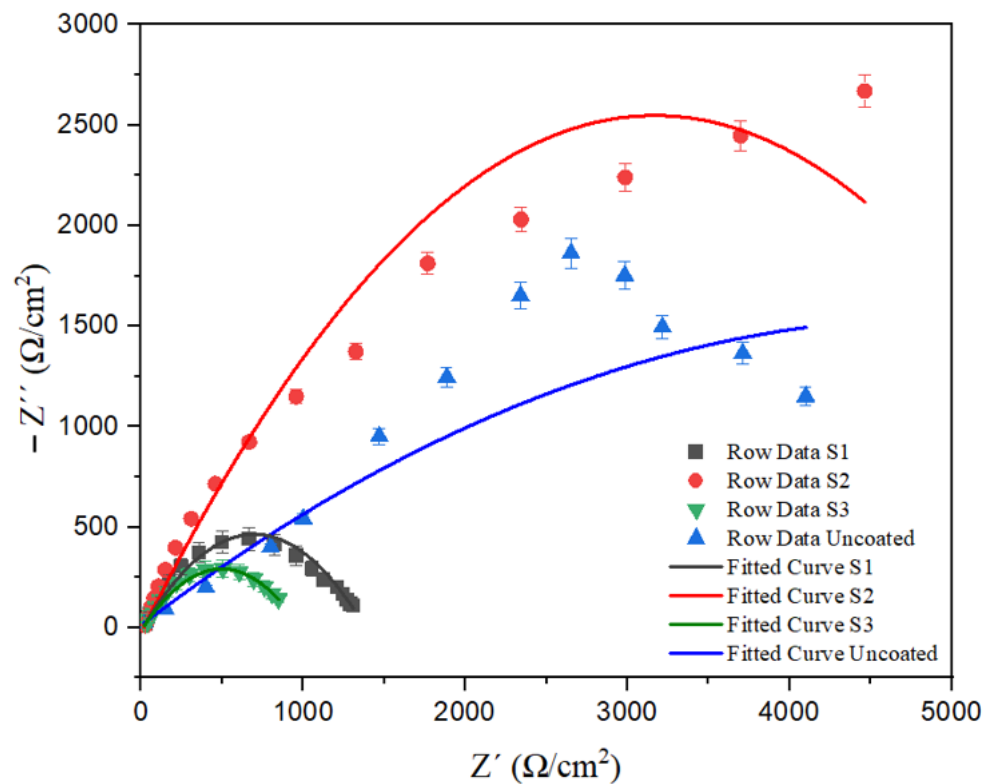


Figure 7. Nyquist diagrams of different samples in 3.5% NaCl solution at room temperature.

In the equivalent circuit shown in Figure 8 (as selected in ZView software) and Table 7, R_s is the solution resistor, R_{ct} is the charge transfer resistance, and CPE is the constant phase element. According to the parameters of Table 7, the corrosion resistance increased in S2 sample in the impedance test.

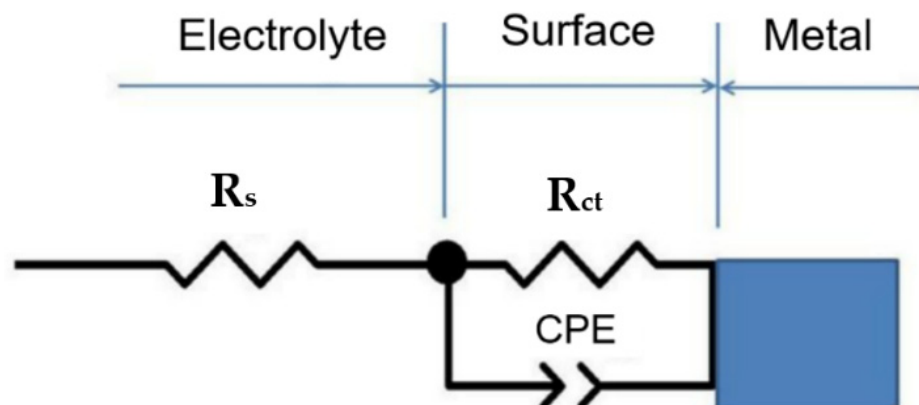


Figure 8. The electrochemical parameters of the circuit are equivalent to different samples [63].

Table 7. The electrochemical parameters of the circuit are equivalent to different samples.

R_{ct} ($\Omega \cdot \text{cm}^{-2}$)	R_s ($\Omega \cdot \text{cm}^{-2}$)	CPE ($\text{Fs}^{n-1} \cdot \text{cm}^{-2}$)	Sample
941	27.65	0.67217	S1
8969	18.83	0.18763	S2
1320	22.52	0.86593	S3
4381	17.04	0.4321	Uncoated

The graph related to the coating of sample S2 has a significant resistance up to the range of 3000 to 3500 Ω/cm^2 . However, the coating resistance started to decrease after some time, indicating the beginning of the corrosion process and the formation of holes. The passive layer on the surface created anti-corrosion properties when the cladding method was used for coating [69]. The graphs related to the Inconel 625 coating of the S1 and S3 samples have assumed a semi-circular state, which indicates a rapid drop in their surface resistance against corrosion. According to previous studies [40], this decrease in resistance in these samples is due to the development of corrosion by chloride ions and as a result of the severe damage of the passive layer due to the penetration of chloride ions. According to the Nyquist curve, the value of R_{ct} for the S1 and S3 samples is lower than the uncoated sample, which, according to the EDS analysis results reported in Table 6, can be attributed to the lower amount of molybdenum and chromium elements in these samples than in the uncoated sample.

Constant phase elements (CPE) are widely used in electrical equivalent circuits to fit experimental impedance data [70]. CPE behaviour is generally attributed to distributed surface reactivity, surface inhomogeneity, roughness or fractal geometry, electrode porosity, and current/potential distributions associated with electrode geometry [71]. The coatings of samples S1, S2, and S3 with high-frequency range for total impedance are shown in Table 7. Sample S2 has passed a lower amount of CPE as the geometry of the etched surface is more regular, and this caused less distribution of stationary-phase elements on the surface (Figure 5) [72].

R_{ct} in the fitted equivalent circuit is related to the charge transfer resistance on the surface of the sample under the impedance test, which indicates the kinetics of charge transfer at the interface between the sample and the corrosive solution and is related to corrosion reactions. The size of the diameter of the semicircle in circuits with one constant phase element indicates the value of R_{ct} . The higher this value is, the lower the kinetics of the corrosion reaction on the surface of the sample, which, as a result, indicates higher corrosion resistance [73]. So, the higher this R_{ct} , the more corrosion-resistant the coating and the lower the corrosion rate. According to Table 7, sample S2 has the highest value of R_{ct} , indicating the greater corrosion resistance of this sample; on the opposite side, sample S1 has the lowest value of R_{ct} , followed by the lowest corrosion resistance. On the other hand, by measuring the diameter of the semicircles in Figure 5, it is also possible to determine the value of R_{ct} in the samples. CPE shows the amount of penetration into the passive layer formed on the samples; with the increase in CPE, the amount of defects in the passive layer on the samples increased. The corrosive solution caused the surface corrosion of the samples to occur more easily. As is clear in Table 7, sample S2 had the lowest amount of CPE and, as a result, the highest amount of corrosion resistance.

Due to the presence of nickel, molybdenum, and niobium—which has different conductivity ratio [74]—sample S2 did not pass much electrical current, increasing the initial resistance of the solution to almost 3500 $\Omega \cdot \text{cm}^{-2}$. Measuring the diameter of the semicircles in Figure 5, it can be verified that the increase in CPE has a direct relationship with the number of defects (cavities) in the passive layer on the samples, and the electrolyte solution caused their surface corrosion.

4. Conclusions

In this study, the aim was to investigate surface corrosion in an Inconel 625 coating. Laser cladding was the selected deposition process, and it was performed with different laser powers on the Inconel 738 substrate. Potentiodynamic polarization (Tafel) and electrochemical impedance tests were performed, and the conclusions are summarized as follows:

1. The cross-sectional images of the coated samples showed that the laser power has a significant influence on the widening of the heat-affected zone (HAZ) and the thickening of the layer attached to the surface.

2. Corrosion morphologies on the surfaces of the samples were pitting and cavity types caused by laser power and surface interactions with the electrolyte (3.5% NaCl).
3. The situated molybdenum and chromium ions within the pores and cavities helped to maintain the protective layer and decreased the corrosion rate.
4. Nickel ions can increase the pH of the electrolyte solution, which induces a faster and easier formation of the passive layer, occupying a larger area according to the electrochemical phase diagram, and consequently reducing the corrosion rate.
5. The lower value of CPE in the electrochemical impedance curve of sample S2 indicated that the corrosion kinetics in this sample is lower than in other samples. This is a result of the fact that a lower current density of the corrosive solution reacts with the surface of the sample.
6. A higher amount of Mo, Cr, and Nb elements in the S2 sample caused a faster and more resistant passive layer in this sample compared to other samples, which led to the superior corrosion resistance of this sample in Tafel and electrochemical impedance tests.

Author Contributions: Author Contributions: Conceptualization, H.B.; Methodology, M.T.N. and M.S.Y.; Software, M.A.M.; Investigation, A.A.S. and M.T.; Data curation, A.M. and M.A.M.; Writing—original draft, M.R.; Writing—review & editing, M.M., A.M.M.G. and H.B.; Visualization, M.R. and M.A.M.; Supervision, M.T.N. and M.S.Y.; Project administration, M.S.Y. All authors have read and agreed to the published version of the manuscript.

Funding: This research was funded by Financial support from the Spanish Government (Agencia Estatal de Investigación) grant number PID2019-106631GB-C41/C42 and PGC2018-096855-B-C41. And The APC was funded by Regional Government of Madrid through the program ADITIMAT (S2018/NMT-4411), Spanish Government for its postdoctoral support (Margarita Salas 2022) and AGAUR, Agency for Administration of University and Research (Agència de Gestió d'Ajuts Universitaris i de Recerca) (2021 SGR 01053).

Institutional Review Board Statement: Not applicable.

Informed Consent Statement: Not applicable.

Data Availability Statement: Not applicable.

Acknowledgments: The authors would like to express their special gratitude to the members of the Center for Structural Integrity, Micromechanics, and Reliability of Materials (CIEFMA), Department of Materials Science and Engineering, for technical support. Moreover, the authors acknowledge the financial support from the Spanish Government (Agencia Estatal de Investigación) through the projects PID2019-106631GB-C41/C42 (AEI/10.13039/501100011033) and PGC2018-096855-B-C41, and the Regional Government of Madrid through the program ADITIMAT, ref. S2018/NMT-4411. M. Rezayat acknowledges the AGAUR (FI-SDUR-2020) of the Generalitat de Catalunya for its financial support. H. Besharatloo appreciates the Spanish Government for its postdoctoral support through Margarita Salas grants.

Conflicts of Interest: The authors declare no conflict of interest.

References

1. Jonsta, Z.; Jonsta, P.; Konecna, K.; Gabcova, M. Phase Analysis of Nickel Superalloy Inconel 738 LC. *Commun.-Sci. Lett. Univ. Zilina* **2010**, *12*, 90–94. [[CrossRef](#)]
2. Gurrappa, I.; Yashwanth, I.; Mounika, I.; Murakami, H.; Kuroda, H.M.A.S. The Importance of Hot Corrosion and Its Effective Prevention for Enhanced Efficiency of Gas Turbines. *Gas Turbines-Mater. Model. Perform.* **2015**, *1*, 55–102. [[CrossRef](#)]
3. Aina, J.O.; Ojo, O.A.; Chaturvedi, M.C. Enhanced laser weldability of an aerospace superalloy by thermal treatment. *Sci. Technol. Weld. Join.* **2018**, *24*, 225–234. [[CrossRef](#)]
4. Rezayat, M.; Yazdi, M.S.; Zandi, M.D.; Azami, A. Tribological and corrosion performance of electrodeposited Ni-Fe/Al₂O₃ coating. *Results Surf. Interfaces* **2022**, *9*, 100083. [[CrossRef](#)]
5. Ghanavati, R.; Naffakh-Moosavy, H.; Moradi, M. Additive manufacturing of thin-walled SS316L-IN718 functionally graded materials by direct laser metal deposition. *J. Mater. Res. Technol.* **2021**, *15*, 2673–2685. [[CrossRef](#)]
6. Ramakrishnan, A.; Dinda, G. Direct laser metal deposition of Inconel 738. *Mater. Sci. Eng. A* **2019**, *740–741*, 1–13. [[CrossRef](#)]

7. Zhang, F.; Levine, L.E.; Allen, A.J.; Stoudt, M.R.; Lindwall, G.; Lass, E.A.; Williams, M.E.; Idell, Y.; Campbell, C.E. Effect of heat treatment on the microstructural evolution of a nickel-based superalloy additive-manufactured by laser powder bed fusion. *Acta Mater.* **2018**, *152*, 200–214. [[CrossRef](#)] [[PubMed](#)]
8. Mashhuriazar, A.; Gur, C.H.; Sajuri, Z.; Omidvar, H. Effects of heat input on metallurgical behavior in HAZ of multi-pass and multi-layer welded IN-939 superalloy. *J. Mater. Res. Technol.* **2021**, *15*, 1590–1603. [[CrossRef](#)]
9. Abedi, H.; Ojo, O. Enhanced resistance to gas tungsten arc weld heat-affected zone cracking in a newly developed Co-based superalloy. *Mater. Sci. Eng. A* **2022**, *851*, 143618. [[CrossRef](#)]
10. Jasim, A.H.; Abid-Ali, A.R.K.; Mahboubi, F. Coating Process on Inconel Super alloy Substrates: A Review. *J. Phys. Conf. Ser.* **2021**, *1973*, 012086. [[CrossRef](#)]
11. Shankar, V.; Rao, K.B.S.; Mannan, S. Microstructure and mechanical properties of Inconel 625 superalloy. *J. Nucl. Mater.* **2001**, *288*, 222–232. [[CrossRef](#)]
12. Co, M.I. Shot peening applications. *Met. Finish.* **2006**, *104*, 73.
13. Yazdi, M.S.; Rezayat, M.; Rovira, J.J.R. ElectroCatalytic Activity of Nickel Foam with Co, Mo, and Ni Phosphide Nanostructures. *Plasma* **2022**, *5*, 221–232. [[CrossRef](#)]
14. Seleznev, A.; Pinargote, N.; Smirnov, A. Machinability of Nickel-Based Superalloys Using Ceramic Tools. *Metals* **2021**, *11*, 1385. [[CrossRef](#)]
15. Hastuty, S.; Zacharias, P.; Awwaluddin, M.; Krismawan; Setiawan, P.H.; Siswanto, E.; Santoso, B.; Nugroho, A.; Abdul-Rani, A.M. Considerations of Material Selection for Control Rod Drive Mechanism of Reaktor Daya Eksperimental. *J. Phys. Conf. Ser.* **2019**, *1198*, 032010. [[CrossRef](#)]
16. Votruba, V.; Diviš, I.; Pilsová, L.; Zeman, P.; Beránek, L.; Horváth, J.; Smolík, J. Experimental investigation of CMT discontinuous wire arc additive manufacturing of Inconel 625. *Int. J. Adv. Manuf. Technol.* **2022**, *122*, 711–727. [[CrossRef](#)]
17. Grünling, H.; Schneider, K.; Singheiser, L. Mechanical Properties of coated systems. *Mater. Sci. Eng.* **1987**, *88*, 177–189. [[CrossRef](#)]
18. Egbewande, A.T.; Zhang, H.; Sidhu, R.K.; Ojo, O.A. Improvement in Laser Weldability of INCONEL 738 Superalloy through Microstructural Modification. *Met. Mater. Trans. A* **2009**, *40*, 2694–2704. [[CrossRef](#)]
19. Fantozzi, D.; Matikainen, V.; Uusitalo, M.; Koivuluoto, H.; Vuoristo, P. Chlorine-induced high temperature corrosion of Inconel 625 sprayed coatings deposited with different thermal spray techniques. *Surf. Coat. Technol.* **2017**, *318*, 233–243. [[CrossRef](#)]
20. Oladijo, O.; Luzin, V.; Ntsoane, T. Thermally Sprayed Inconel 625 Coating on 304 Stainless Steel: A Neutron Diffraction Stress Analysis. *Procedia Manuf.* **2019**, *35*, 1234–1239. [[CrossRef](#)]
21. Fotovvati, B.; Namdari, N.; Dehghanghadikolaei, A. On Coating Techniques for Surface Protection: A Review. *J. Manuf. Mater. Process.* **2019**, *3*, 28. [[CrossRef](#)]
22. Figueira, R.M.B.B.M.; Fontinha, I.R.; Silva, C.J.R.; Pereira, E.V. Hybrid Sol-Gel Coatings: Smart and Green Materials for Corrosion Mitigation. *Coatings* **2016**, *6*, 12. [[CrossRef](#)]
23. Arbuzova, S.S.; Butyagin, P.I.; Bol'Shanin, A.V.; Kondratenko, A.I.; Vorob'Ev, A.V. Microarc Oxidation of Metal Surfaces: Coating Properties and Applications. *Russ. Phys. J.* **2020**, *62*, 2086–2091. [[CrossRef](#)]
24. Rezayat, M.; Yazdi, M.S.; Noghani, M.T.; Ahmadi, R. Bactericidal Properties of Copper-Tin Nanoparticles on *Escherichia coli* in a Liquid Environment. *Plasma* **2020**, *3*, 153–165. [[CrossRef](#)]
25. Kowalczyk, P.; Dybowski, K.; Januszewicz, B.; Atraszkiewicz, R.; Makówka, M. The Hybrid Process of Low-Pressure Carburizing and Metallization (Cr + LPC, Al + LPC) of 17CrNiMo7-6 and 10NiCrMo13-5 Steels. *Coatings* **2021**, *11*, 567. [[CrossRef](#)]
26. Zhang, Q.; Wang, L.; Mei, X.; Yao, J. Development of Laser Surface Modification Technology. *Chin. J. Eng. Sci.* **2020**, *22*, 71–77. [[CrossRef](#)]
27. Xue, T.; Attarilar, S.; Liu, S.; Liu, J.; Song, X.; Li, L.; Zhao, B.; Tang, Y. Surface Modification Techniques of Titanium and its Alloys to Functionally Optimize Their Biomedical Properties: Thematic Review. *Front. Bioeng. Biotechnol.* **2020**, *8*, 603072. [[CrossRef](#)] [[PubMed](#)]
28. Li, C.; Xu, X.; Wang, S.; Tabie, V.M.; Yang, S.; Zhang, T.; Liu, Y. High-temperature oxidation and hot corrosion behavior of the Cr-modified aluminide coating obtained by a Thermal Diffusion process. *Mater. Res. Express* **2019**, *6*, 086444. [[CrossRef](#)]
29. Taheri, M.; Kashani-Bozorg, S.F.; Ramalingam, V.V.; Babaei, B.; Halvae, A. Effect of Nd:YAG Pulsed-Laser Welding Parameters on Melting Rate of GTD-111 Superalloy Joint. *J. Mater. Eng. Perform.* **2021**, *30*, 9108–9117. [[CrossRef](#)]
30. John, M.; Kuruveri, U.B.; Menezes, P.L. Laser Cladding-Based Surface Modification of Carbon Steel and High-Alloy Steel for Extreme Condition Applications. *Coatings* **2022**, *12*, 1444. [[CrossRef](#)]
31. Jain, A.; Kumari, N.; Jagadevan, S.; Bajpai, V. Surface properties and bacterial behavior of micro conical dimple textured Ti6Al4V surface through micro-milling. *Surf. Interfaces* **2020**, *21*, 100714. [[CrossRef](#)]
32. Safari, M.; Moradi, M.; Joudaki, J.; Babaei, A.M. Experimental investigation of laser cladding of H13 hot work steel by Stellite 6 powder. *Sādhanā* **2022**, *47*, 144. [[CrossRef](#)]
33. Muller, P.; Mognol, P.; Hascoet, J.-Y. Modeling and control of a direct laser powder deposition process for Functionally Graded Materials (FGM) parts manufacturing. *J. Mater. Process. Technol.* **2013**, *213*, 685–692. [[CrossRef](#)]
34. Niu, X.; Singh, S.; Garg, A.; Singh, H.; Panda, B.; Peng, X.; Zhang, Q. Review of materials used in laser-aided additive manufacturing processes to produce metallic products. *Front. Mech. Eng.* **2018**, *14*, 282–298. [[CrossRef](#)]
35. Ahn, D.-G. Directed Energy Deposition (DED) Process: State of the Art. *Int. J. Precis. Eng. Manuf.-Green Technol.* **2021**, *8*, 703–742. [[CrossRef](#)]

36. Mondal, K.; Nuñez, L.; Downey, C.M.; van Rooyen, I.J. Thermal Barrier Coatings Overview: Design, Manufacturing, and Applications in High-Temperature Industries. *Ind. Eng. Chem. Res.* **2021**, *60*, 6061–6077. [[CrossRef](#)]
37. Selvaraj, S.K.; Srinivasan, K.; Deshmukh, J.; Agrawal, D.; Mungilwar, S.; Jagtap, R.; Hu, Y.-C. Performance Comparison of Advanced Ceramic Cladding Approaches via Solid-State and Traditional Welding Processes: A Review. *Materials* **2020**, *13*, 5805. [[CrossRef](#)] [[PubMed](#)]
38. Cabrini, M.; Lorenzi, S.; Testa, C.; Pastore, T.; Brevi, F.; Biamino, S.; Fino, P.; Manfredi, D.; Marchese, G.; Calignano, F.; et al. Evaluation of Corrosion Resistance of Alloy 625 Obtained by Laser Powder Bed Fusion. *J. Electrochem. Soc.* **2019**, *166*, C3399–C3408. [[CrossRef](#)]
39. Wang, M.; Zeng, S.; Zhang, H.; Zhu, M.; Lei, C.; Li, B. Corrosion behaviors of 316 stainless steel and Inconel 625 alloy in chloride molten salts for solar energy storage. *High Temp. Mater. Process.* **2020**, *39*, 340–350. [[CrossRef](#)]
40. Abe, F.; Osakada, K.; Shiomi, M.; Uematsu, K.; Matsumoto, M. The manufacturing of hard tools from metallic powders by selective laser melting. *J. Mater. Process. Technol.* **2001**, *111*, 210–213. [[CrossRef](#)]
41. Baboian, R. *Corrosion Tests and Standards*; ASTM International: West Conshohocken, PA, USA, 2005.
42. Verdi, D.; Garrido, M.; Múñez, C.; Poza, P. Cr3C2 incorporation into an Inconel 625 laser clad coating: Effects on matrix microstructure, mechanical properties and local scratch resistance. *Mater. Des.* **2015**, *67*, 20–27. [[CrossRef](#)]
43. Badtke, M.; Tanaka, H.; Kalusniak, S.; Demesh, M.; Kuleshov, N.; Kränkel, C. Few-ns, kW peak power Q-switched pulses from orange and red Pr:YLF lasers. *Appl. Phys. Express* **2022**, *15*, 082006. [[CrossRef](#)]
44. Odabaşı, A.; Ünlü, N.; Goller, G.; Eruslu, M.N. A Study on Laser Beam Welding (LBW) Technique: Effect of Heat Input on the Microstructural Evolution of Superalloy Inconel 718. *Met. Mater. Trans. A* **2010**, *41*, 2357–2365. [[CrossRef](#)]
45. Shi, Y.; Zhou, X.; Wang, X.; Feng, X.; Peng, L. Effects of Electromagnetic Fields on the Microstructure of Laser Cladding. *Materials* **2022**, *15*, 4198. [[CrossRef](#)] [[PubMed](#)]
46. Rai, S.K.; Kumar, A.; Shankar, V.; Jayakumar, T.; Rao, K.B.S.; Raj, B. Characterization of microstructures in Inconel 625 using X-ray diffraction peak broadening and lattice parameter measurements. *Scr. Mater.* **2004**, *51*, 59–63. [[CrossRef](#)]
47. Sarkar, A.; Mukherjee, P.; Barat, P.; Jayakumar, T.; Mahadevan, S.; Rai, S.K. Lattice Misfit Measurement in Inconel 625 by X-ray Diffraction Technique. *Int. J. Mod. Phys. B* **2008**, *22*, 3977–3985. [[CrossRef](#)]
48. Abioye, T.; McCartney, D.; Clare, A. Laser cladding of Inconel 625 wire for corrosion protection. *J. Mater. Process. Technol.* **2015**, *217*, 232–240. [[CrossRef](#)]
49. Schmeiser, F.; Krohmer, E.; Wagner, C.; Schell, N.; Uhlmann, E.; Reimers, W. In situ microstructure analysis of Inconel 625 during laser powder bed fusion. *J. Mater. Sci.* **2021**, *57*, 9663–9677. [[CrossRef](#)]
50. Schröder, J.; Evans, A.; Polatidis, E.; Čapek, J.; Mohr, G.; Serrano-Munoz, I.; Bruno, G. Understanding the impact of texture on the micromechanical anisotropy of laser powder bed fused Inconel 718. *J. Mater. Sci.* **2022**, *57*, 15036–15058. [[CrossRef](#)]
51. Cortial, F.; Corrieu, J.M.; Vernot-Loier, C. Influence of heat treatments on microstructure, mechanical properties, and corrosion resistance of weld alloy 625. *Met. Mater. Trans. A* **1995**, *26*, 1273–1286. [[CrossRef](#)]
52. Zhang, D.; Harris, S.; McCartney, D. Microstructure formation and corrosion behaviour in HVOF-sprayed Inconel 625 coatings. *Mater. Sci. Eng. A* **2003**, *344*, 45–56. [[CrossRef](#)]
53. Yin, Z.; Zhao, W.; Lai, W.; Zhao, X. Electrochemical behaviour of Ni-base alloys exposed under oil/gas field environments. *Corros. Sci.* **2009**, *51*, 1702–1706. [[CrossRef](#)]
54. Sridhar, N. Models for predicting corrosion. *Tech. Corros. Monit.* **2008**, 499–538. [[CrossRef](#)]
55. Kozaderov, O.; Światowska, J.; Dragoe, D.; Burliaev, D.; Volovitch, P. Effect of Cr(III) passivation layer on surface modifications of zinc-nickel coatings in chloride solutions. *J. Solid State Electrochem.* **2021**, *25*, 1161–1173. [[CrossRef](#)]
56. Li, W.; Cao, R.; Xu, L.; Qiao, L. The role of hydrogen in the corrosion and cracking of steels—A review. *Corros. Commun.* **2021**, *4*, 23–32. [[CrossRef](#)]
57. Salarvand, V.; Sohrabpoor, H.; Mohammadi, M.; Nazari, M.; Raghavendra, R.; Mostafaei, A.; Brabazon, D. Microstructure and corrosion evaluation of as-built and heat-treated 316L stainless steel manufactured by laser powder bed fusion. *J. Mater. Res. Technol.* **2022**, *18*, 4104–4113. [[CrossRef](#)]
58. Lyon, S. Corrosion of Molybdenum and its Alloys. *Shreir's Corros.* **2010**, *3*, 2157–2167. [[CrossRef](#)]
59. Scendo, M.; Staszewska-Samson, K.; Danielewski, H. Corrosion Behavior of Inconel 625 Coating Produced by Laser Cladding. *Coatings* **2021**, *11*, 759. [[CrossRef](#)]
60. Gui, W.; Zhong, C.; Gu, J.; Ding, Y.; Wang, X.; Wu, T.; Liang, Y.; Qin, J.; Qu, Y.; Lin, J. Laser-clad Inconel 625 coatings on Q245R structure steel: Microstructure, wear and corrosion resistance. *NPJ Mater. Degrad.* **2022**, *6*, 37. [[CrossRef](#)]
61. Bakkar, A.; Ahmed, M.M.; Alsaleh, N.; Seleman, M.M.E.-S.; Ataya, S. Microstructure, wear, and corrosion characterization of high TiC content Inconel 625 matrix composites. *J. Mater. Res. Technol.* **2018**, *8*, 1102–1110. [[CrossRef](#)]
62. May, Z.; Alam, K.; Nayan, N.A. Recent Advances in Nondestructive Method and Assessment of Corrosion Undercoating in Carbon-Steel Pipelines. *Sensors* **2022**, *22*, 6654. [[CrossRef](#)]
63. Zhang, B.; Xiu, M.; Tan, Y.T.; Wei, J.; Wang, P. Pitting corrosion of SLM Inconel 718 sample under surface and heat treatments. *Appl. Surf. Sci.* **2019**, *490*, 556–567. [[CrossRef](#)]
64. Cook, W.G.; Olive, R.P. Pourbaix diagrams for chromium, aluminum and titanium extended to high-subcritical and low-supercritical conditions. *Corros. Sci.* **2012**, *58*, 291–298. [[CrossRef](#)]

65. Selvig, A.; Huang, X.; Kim, D.J.; Guzonas, D. Surface oxide formation on IN625 and plasma sprayed NiCrAlY after high density and low density supercritical water testing. *Mater. Corros.* **2012**, *65*, 768–777. [[CrossRef](#)]
66. Matulis, J.; Sližys, R. On some characteristics of cathodic processes in nickel electrodeposition. *Electrochim. Acta* **1964**, *9*, 1177–1188. [[CrossRef](#)]
67. Asselin, E.; Alfantazi, A.; Rogak, S. A Polarization Study of Alloy 625, Nickel, Chromium, and Molybdenum in Ammoniated Sulfate Solutions. *Corrosion* **2005**, *61*, 579–586. [[CrossRef](#)]
68. Fesharaki, M.N.; Razavi, R.S.; Mansouri, H.A.; Jamali, H. Microstructure investigation of Inconel 625 coating obtained by laser cladding and TIG cladding methods. *Surf. Coat. Technol.* **2018**, *353*, 25–31. [[CrossRef](#)]
69. Fesharaki, M.N.; Razavi, R.S.; Mansouri, H.A.; Jamali, H. Evaluation of the hot corrosion behavior of Inconel 625 coatings on the Inconel 738 substrate by laser and TIG cladding techniques. *Opt. Laser Technol.* **2019**, *111*, 744–753. [[CrossRef](#)]
70. Holm, S.; Holm, T.; Martinsen, Ø.G. Simple circuit equivalents for the constant phase element. *PLoS ONE* **2021**, *16*, e0248786. [[CrossRef](#)]
71. Pajkossy, T. Electrochemistry of Fractal Surfaces. *Encycl. Interfacial Chem.* **2018**, 121–124. [[CrossRef](#)]
72. Jorcin, J.-B.; Orazem, M.E.; Pébère, N.; Tribollet, B. CPE analysis by local electrochemical impedance spectroscopy. *Electrochim. Acta* **2006**, *51*, 1473–1479. [[CrossRef](#)]
73. Wang, L.; Li, H.; Liu, Q.; Xu, L.; Lin, S.; Zheng, K. Effect of sodium chloride on the electrochemical corrosion of Inconel 625 at high temperature and pressure. *J. Alloys Compd.* **2017**, *703*, 523–529. [[CrossRef](#)]
74. Eliaz, N. Corrosion of Metallic Biomaterials: A Review. *Materials* **2019**, *12*, 407. [[CrossRef](#)] [[PubMed](#)]

Disclaimer/Publisher’s Note: The statements, opinions and data contained in all publications are solely those of the individual author(s) and contributor(s) and not of MDPI and/or the editor(s). MDPI and/or the editor(s) disclaim responsibility for any injury to people or property resulting from any ideas, methods, instructions or products referred to in the content.